Japanese Journal of Applied Physics
Vol. 46, No. 7A, 2007, pp. 4395–4402

Apparent Topographic Height Variations Measured by Noncontact Atomic Force Microscopy

Kai-Ming YANG, Jen-Yang CHUNG, Ming-Feng HSIEH, and Deng-Sung LIN*

Institute of Physics, National Chiao-Tung University, 1001 Ta-Hsueh Road, Hsinchu 30010, Taiwan

(Received February 14, 2007; accepted April 7, 2007; published online July 4, 2007)

The topographic height measurement on a sample consisting of domains of different materials in noncontact atomic force microscopy (NC-AFM) is typically incorrect owing to the variation in electrostatic force between a tip and a sample. The tip–sample electrostatic force is owing to the difference in effective contact potential between a tip and a sample. This study demonstrates that the error in height strongly depends on the bias applied between the tip and the sample, the radius of the tip apex, the work function difference, and the frequency shift. Experimental results are well explained by integrated model calculations and by including the van der Waals and electrostatic forces between the tip and the sample in the analysis. When the simultaneous compensation of contact potentials during imaging is not performed, the errors occurring in the height measurement can be estimated from the tip–sample distance vs the bias curves obtained *in situ*.
[DOI: 10.1143/JJAP.46.4395]

KEYWORDS: NC-AFM, thin silicon oxide film, contact potential

1. Introduction

Atomic force microscopy (AFM) has been routinely used in numerous scientific and technological areas. Particularly, noncontact AFM (NC-AFM) performed in a vacuum environment can successfully image delicate structures, which may easily be altered by the force exerted in contact AFM, and is frequently employed for applications requiring a high resolution.[1–4] In NC-AFM, the forces between a macroscopic nonmagnetic tip and a nonmagnetic sample, F_{ts}, involve the chemical, van der Waals, and electrostatic forces. Despite the fact that these forces have different physical origins and involve complex many-body problems, ultrahigh-vacuum NC-AFM still enables the imaging the solid surfaces of both conducting and nonconducting materials at a true atomic resolution.

Different tip–sample forces enable various NC-AFM operation modes as well as spectroscopy and other measurements in addition to topography. On the other hand, the dependencies of these forces on the tip size, shape, and material also add to the complexity of the analysis and interpretation of various images. One example is that the relative topographic height measurements between two regions of different materials on a sample by NC-AFM can substantially deviate from their true values because the tip is subject to different electrostatic forces on the surfaces of the two materials.[5–9] Between conducting tips and samples, the residual electrostatic force originates from contact potential differences and is proportional to the capacitance gradient of the tip–sample system,

$$F_{es} = -\frac{1}{2}\frac{dC}{dz}V^2 = -\frac{1}{2}\frac{dC}{dz}(V_a + V_b + V_{cp})^2, \quad (1.1)$$

where C and V are the effective capacitance and net potential difference, respectively. For a conducting sample, the net potential difference V consists of three terms: the contact potential difference V_{cp} between the tip and the sample, the applied tip bias voltage V_a, and the built-in bias V_b for any stray charges that may exist locally in some tip/sample areas.[10,11] Often the sample systems subjected to NC-AFM topographic imaging consist of several materials with different contact potentials. The electrostatic contributions on top of the materials are different owing to the change in V_{cp} over the surface areas of the materials. Consequently, the topographic height measurement on these sample systems shows variations. Sadewasser and coworkers studied this issue and showed that the correct height measurement on samples with only two different contact potentials (V_{cp1} and V_{cp2}) is possible by adjusting the bias voltage applied to compensate for the different contact potentials and that the desired applied bias voltage is the negative of the mean voltage V_{mcp} of the two contact potentials: $V_a = -V_{mcp} = -(V_{cp1} + V_{cp2})/2$.[5,6] In their study, the effect of the electrostatic force on the topographic height measurement is also simulated without the van der Waals force and a cone-shaped tip model is considered to describe their results well.

In this study, we investigated in detail the height deviation in frequency-modulated NC-AFM for two test sample systems consisting of domains of different materials for tips of various sizes and with external bias. When a contact potential is not completely compensated under typical imaging conditions, our results show that height variations depend strongly on the radius, bias polarity, bias, frequency shift, and conducting state of the tip. Whereas the dependence of topographic height measurement on these variables is expected, the detailed functional dependence between the height measurement and these variables is not obvious. We integrated several successful formulations, which were previously developed for describing tip–sample forces and system responses, to explain complex functional relationships. Our observations are well explained by numerical modeling accounting for all essential interactions and geometrical effects. The obtained results illustrate the interplay of different forces that must be considered for the complete understanding of AFM and provide a systematic method for estimating the deviation in height measurement *in situ*.

2. Experimental Methods

In our experiment, scanning tunneling microscopy (STM) and NC-AFM measurements were performed in an ultrahigh-vacuum chamber, which had a basic pressure of 8×10^{-11} Torr and was equipped with a commercial variable-

*E-mail address: dslin@mail.nctu.edu.tw

temperature STM/NC-AFM system. Commercial heavily doped monolithic Si cantilevers with an initial tip radius of ~7 nm were used. The force constant k of the cantilevers was ~42 N/m and their free resonance frequency f_0 was ~260 kHz. Conductive tips had an additional 25-nm-thick double-layered structure consisting of chromium and $PtIr_5$. The physical parameters for the tips used in the experiment were extracted from manufacturing specifications and our own measurements of the tips. All images in this study were obtained at a cantilever oscillation amplitude (A) of ~16 nm.

The samples used for patterning neighboring n- and p-doped regions were lightly n-doped Si(100) wafers with a phosphorus doping concentration of $3 \times 10^{14}\,\mathrm{cm}^{-3}$. Standard ion-implantation and photolithographic techniques for semiconductor manufacturing were employed to create the patterns of heavily p-doped regions with boron as the implanted impurity at a concentration of $10^{18}\,\mathrm{cm}^{-3}$. The samples were annealed to remove implantation damage, acid-etched, and then terminated with hydrogen immediately before their insertion into the measurement chamber. Si(111) samples were cut from boron-doped p-type wafers and cleaned by standard direct Joule heating to ~1450 K for 10 s after thorough outgassing at 900 K. This standard procedure leads to a (7×7) reconstruction. Thermal oxidation on a clean Si(111)-(7×7) surface was performed *in situ* at a substrate temperature of ~1000 K and an O_2 gas pressure of 2×10^{-5} Torr for 300 s. This procedure typically results in an amorphous oxide film of around 0.5 nm thickness.[12] Sample heating was achieved by adjusting the direct DC current.

3. Results and Discussion

3.1 *Relevant forces and force gradients*

The total forces between a nonmagnetic tip and a conducting sample are commonly categorized into the short-ranged chemical force F_{chem}, van der Waals force F_{vdW}, and long-ranged electrostatic force F_{es}, i.e., $F_{\mathrm{ts}} = F_{\mathrm{chem}} + F_{\mathrm{es}} + F_{\mathrm{vdW}}$. The chemical force, due to the formation of bonds between the tip and sample atoms, is compatible with other forces only when the tip–sample distance $z < 0.5$ nm.[13] The obtained frequency shift–distance curves (not shown here) suggested that the minimum tip–sample distance (D) in this study approximately ranges from 1 to 7 nm, and therefore, the chemical force is not relevant. The electrostatic interaction is difficult to analyze owing to its strong tip-shape dependence and was previously modeled by several research groups with different tip geometries.[14–17] Among these research groups, Colchero *et al.* found an analytical formula for a realistic tip shape, i.e., a truncated macroscopic conical tip with a half-angle tip with a nanometer-sized paraboloidal tip apex of radius R. Adopting their analytical formula, the force between a conducting tip structure and a sample, $F_{\mathrm{ts}} = F_{\mathrm{apex}} + F_{\mathrm{cone}} + F_{\mathrm{lever}} + F_{\mathrm{vdW}}$, includes four terms. The first term is the Coulomb force derived from the tip apex. The second term comes from the tip body, which is approximately in the shape of a truncated cone. The third term comes from the cantilever. The force gradient of F_{lever} is negligible.[14] The fourth term is the van der Waals force. It is dominated by the tip apex. F_{apex} and F_{cone} depend on the net potential difference V between the tip and the sample, but F_{vdW} does not. The van der Waals force between the tip and the sample is found to be dominated by the spherical cap with radius R over an infinite surface: $F_{\mathrm{vdW}} = -HR/6z^2$, where z is the tip–sample distance and H is the Hamaker constant.[13,18] In all cases, the tip–sample force can be expressed as $F_{\mathrm{ts}}(z) = F_{\mathrm{apex}} + F_{\mathrm{cone}} + F_{\mathrm{vdW}}$. Explicit expressions for F_{apex} and F_{cone} can be found in ref. 14.

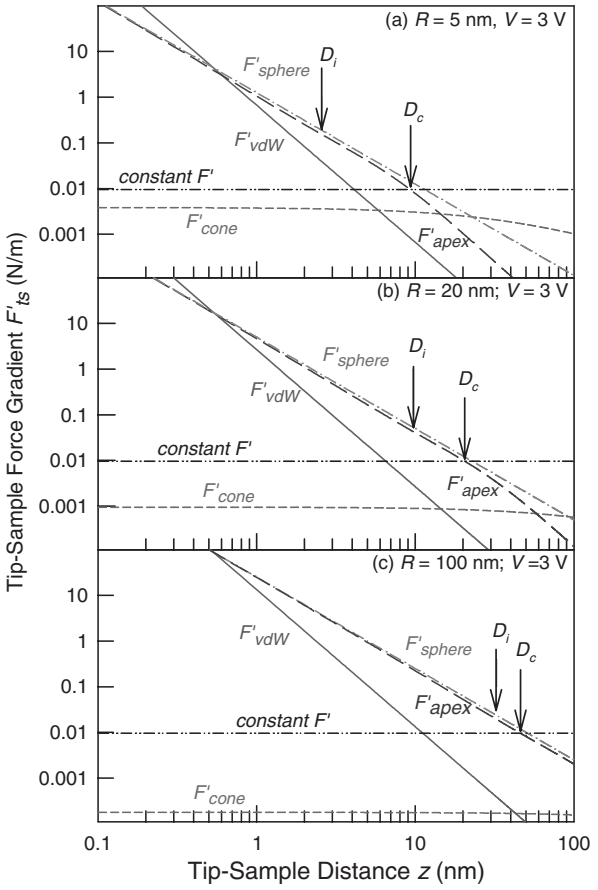

Fig. 1. Log–log scale plot of various tip–sample force gradients with tip radii R = (a) 5, (b) 20, (c) 100 nm. D_c and D_i indicate the minimum tip–sample distances for $\Delta f = -30$ Hz obtained by solving eq. (3.2) (constant force gradient model) and eq. (3.3) (weighted integral model), respectively. The forces were calculated for $H = 4 \times 10^{-19}$ J, $V = 2.5$ V, $R = 25$ nm, and $h = 10\,\mu$m.

The magnitudes of these forces and their gradients are calculated and the force gradients are shown on a log-log scale in Fig. 1. The straightness of curves in Fig. 1 shows that the force-distance curves approximately follow simple power-law relationship. Independent of V, the van der Waals force falls off as the square of tip–sample distance as expected. The force on the truncated cone F_{cone} integrated over the macroscopic shape of the tip is less sensitive to the tip–sample distance. Because large tip apexes lead to a marked truncation of the cone, the force on the tip apex F_{apex} increases with R at the expense of F_{cone}. This is particularly true at a small tip–sample distance, where F_{apex} approaches the force on a simple spherical tip, F_{sphere}, with the effective radius R_{eff}:[16]

$$F_{\mathrm{sphere}} = -\frac{\pi\varepsilon_0 R_{\mathrm{eff}} V^2}{z}. \tag{3.1}$$

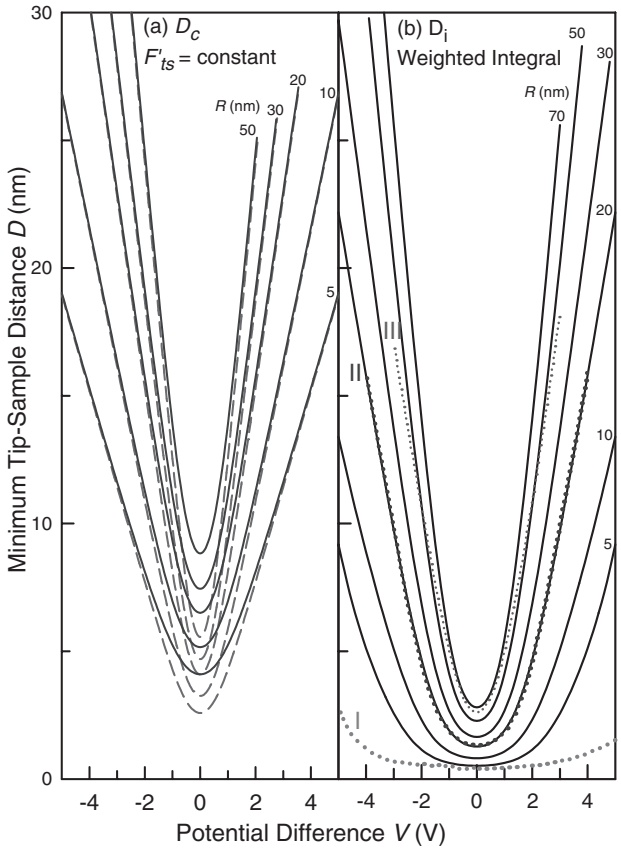

Fig. 2. Minimum tip–sample distances. (a) D_c solved from eq. (3.2) and (b) D_i from eq. (3.3) for $f_0 = 260\,\text{kHz}$, $\Delta f = -30\,\text{Hz}$, $k = 42\,\text{N/m}$, and various tip radii R. The solid and dashed curves in (a) were obtained with $H = 4 \times 10^{-19}$ and $1 \times 10^{-19}\,\text{J}$, respectively. In (b), the dotted curves show the measured minimum tip–sample distance curves at spots above Si areas for tips I–III. The minimum tip sample distances of the measured curves at $V = 0$ were estimated from the Δf–z curves.[24] The corresponding curves obtained above SiO_2 areas have similar line shapes aside from the difference in V_{cp}.

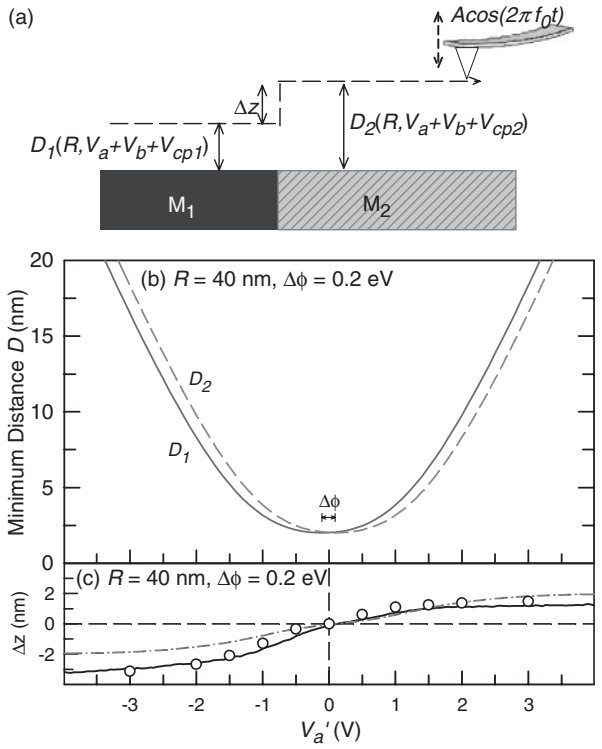

Fig. 3. (a) Schematic diagram showing line profile when tip scans over flat conducting surface. The sample surface has two regions M_1 and M_2 with different work functions ϕ_1 and ϕ_2. (b) Minimum tip–sample distances D_1 and D_2 as function of V'_a on M_1 (solid curve) and M_2 (dashed curve), respectively, calculated for $R = 40\,\text{nm}$ and $\Delta\phi = 0.2\,\text{eV}$. (c) $\Delta z(R, V'_a)$ obtained from AFM images (circles) and by considering differences in $D(R, V)$ in the n- and p-regions obtained by measurement (solid curves) and calculation (dash-dot).

3.2 *Calculation of tip–sample distance*

In the vacuum environment, NC-AFM enables the measurement of the topology of surfaces typically in a frequency modulation mode, i.e., the frequency shift Δf with respect to the free resonance frequency f_0 of the cantilever is kept constant by the feedback control of the minimum tip–sample distance $z_{\min} = D$ (relative height or apparent topological height). Assuming that the force gradient is constant during the oscillation cycle, the frequency shift is proportional to the constant force gradient $F'_{ts}(D)$:[2,4]

$$\Delta f = -\frac{F'_{ts} f_0}{2k}. \tag{3.2}$$

Calculated for $V = 3\,\text{V}$, $f_0 = 260\,\text{kHz}$, $\Delta f = -30\,\text{Hz}$, and $k = 42\,\text{N/m}$, the force gradient F'_{ts} is $9.7 \times 10^{-3}\,\text{N/m}$ and is denoted by the dashed lines in Fig. 1. When the magnitude of the potential difference V and the tip radius increase, F'_{es} and the minimum tip–sample distance D increase in order to keep the frequency shift constant. Accordingly, $D(R, V)$ can be uniquely solved for each V and R. The obtained results are shown in Fig. 2(a) for various apex radii R. For a tip with the given radius R and applied bias V_a, D for any tip position (x, y) over a sample surface can be uniquely solved from eq. (3.2) if the effective local tip–sample contact potential $V_{cp}(x, y)$ is known. The topographic height image $D_c(x, y)$ obtained in the constant frequency-shift mode thus represents the contour of the constant force gradient F'_{ts}.

The gradients of the van der Waals and electrostatic forces between the tip apex and the sample decrease rapidly with an increase in tip–sample distance, as shown in Fig. 1. The amplitude employed in most experiments is actually not sufficiently small for this approximation to hold. By utilizing the Canonical perturbation theory, the frequency shift as a function of D is considered related to the weighted average force over an oscillation cycle:[4]

$$\Delta f = -\frac{{f_0}^2}{kA} \times \int_0^{1/f_0} F_{ts}(D + A + A\cos(2\pi f_0 t))\cos(2\pi f_0 t)\,dt, \tag{3.3}$$

where $A\cos(2\pi f_0 t)$ is the cantilever deflection. Calculated for $f_0 = 260\,\text{kHz}$, $\Delta f = -30\,\text{Hz}$, and $k = 42$, a unique solution D for each V and R can be obtained by solving eq. (3.3); the result $D_i(R, V)$ is shown in Fig. 2(b).

Whereas the curves in both Figs. 2(a) and 2(b) increase with the magnitude of V, the most notable difference between these two figures is that the tip sample distances at $V = 0$, that is, $D(R, V = 0)$ in Fig. 2(a), are larger than those in Fig. 2(b) for the same $H = 4 \times 10^{-19}\,\text{J}$. The frequency shift–distance curves (Δf vs D) suggest that $D(R, V = 0)$ is

near the value observed in Fig. 3(b). The overestimation of D using eq. (3.2) is evident since the calculation uses the largest force gradient observed at the minimum distance for the entire oscillation cycle. Using H smaller than 4×10^{-19} J (and thus a smaller F_{vdW}) effectively inhibits such overestimation, as shown by the dashed curves in Fig. 2(a).

Compared with those in Fig. 2(a), the $D(R, V)$ curves in Fig. 2(b) for small Rs have markedly small curvatures. It is worth noting that F_{apex} and F_{cone} vanish at $V = 0$ and therefore, F_{vdW}, which is independent of V, dominates at $V \approx 0$. As V increases, F_{apex} increases rapidly, the tip retracts, and D_i increases. However, this D_i change is counteracted by F_{vdW}, which diminishes rapidly with increasing D_i. The cone term also increases, but much more slowly, as the distance between the cone and the sample increases. F_{cone} only becomes important at large biases. The counteracting effect of the van der Waals term accounts for the relatively flat response near $V = 0$ for the curves in Fig. 2(b).

3.3 *Origin of incorrect z-height measurement*

To illustrate the origin of the incorrect z-height measurement in NC-AFM, we consider that a tip with an apex of radius $R = 40$ nm and an applied tip bias V_{a} scans over an atomically flat conducting surface, as shown in Fig. 3(a). The sample surface has two regions that consist of materials M_1 and M_2 with the work functions ϕ_1 and ϕ_2, respectively. With the same tip and the same potential difference V, the tip–sample distance is the same in the two domains: $D_1(R, V) = D_2(R, V)$. However, with the same applied voltage V_{a} on the tip, the potential differences between the tip and the two regions, i.e., $V_1 \equiv V_{\mathrm{a}} + V_{\mathrm{b}} + V_{\mathrm{cp1}}$ and $V_2 \equiv V_{\mathrm{a}} + V_{\mathrm{b}} + V_{\mathrm{cp2}}$, are different. The tip–sample distance curves obtained on top of the two regions, that is, $D_1(R, V_1)$ and $D_2(R, V_2)$, are the same except for a horizontal offset of $\Delta V \equiv V_2 - V_1 = V_{\mathrm{cp2}} - V_{\mathrm{cp1}} \equiv \Delta V_{\mathrm{cp}} = \phi_2 - \phi_1 \equiv \Delta\phi$, as shown in Fig. 3(b). Upon scanning laterally with an applied bias V_{a}, a tip experiences a change in potential difference, i.e., ΔV at the domain boundary of M_1 and M_2. Under the same feedback condition, the tip responds to the potential change ΔV by varying the tip–sample distance by a height difference $\Delta z = D(R, V_{\mathrm{a}} + V_{\mathrm{b}} + V_{\mathrm{cp2}}) - D(R, V_{\mathrm{a}} + V_{\mathrm{b}} + V_{\mathrm{cp1}})$, which is plotted as a dash-dot curve in Fig. 3(c). In other words, the topographic height profile shows an apparent height difference Δz between the two domains, even though the surface is actually flat.

When the bias voltage is chosen to compensate for V_{b} and the average of the two contact potentials,

$$V'_{\mathrm{a}} \equiv V_{\mathrm{a}} + V_{\mathrm{b}} + V_{\mathrm{mcp}} = 0, \tag{3.4}$$

where $V_{\mathrm{mcp}} \equiv (V_{\mathrm{cp1}} + V_{\mathrm{cp2}})/2$, one finds

$$\begin{aligned}\Delta z(R, V'_{\mathrm{a}} = 0) &= D\left(R, -\frac{V_{\mathrm{cp2}} - V_{\mathrm{cp1}}}{2}\right) - D\left(R, \frac{V_{\mathrm{cp2}} - V_{\mathrm{cp1}}}{2}\right) \\ &= 0.\end{aligned} \tag{3.5}$$

Thus, the height difference becomes zero for this particular choice of the applied bias; this was confirmed experimentally.[5] Figure 3(c) shows that Δz is an odd function of V'_{a} and the apparent topographic height deviation Δz curve is insignificant near $V'_{\mathrm{a}} = 0$ since the dominating van der Waals force in this region is independent of V and the electrostatic forces are small. As V'_{a} increases, Δz increases with the electrostatic forces and approaches a constant for $V'_{\mathrm{a}} > 2$, where the curves $D(R, V_{\mathrm{a}} + V_{\mathrm{b}} + V_{\mathrm{cp2}})$ and $D(V_{\mathrm{a}} + V_{\mathrm{b}} + V_{\mathrm{cp1}})$ are nearly parallel before F_{cone} becomes dominating at a large V. The apparent topographic height deviation Δz is calculated for various Rs, as shown in Fig. 4.

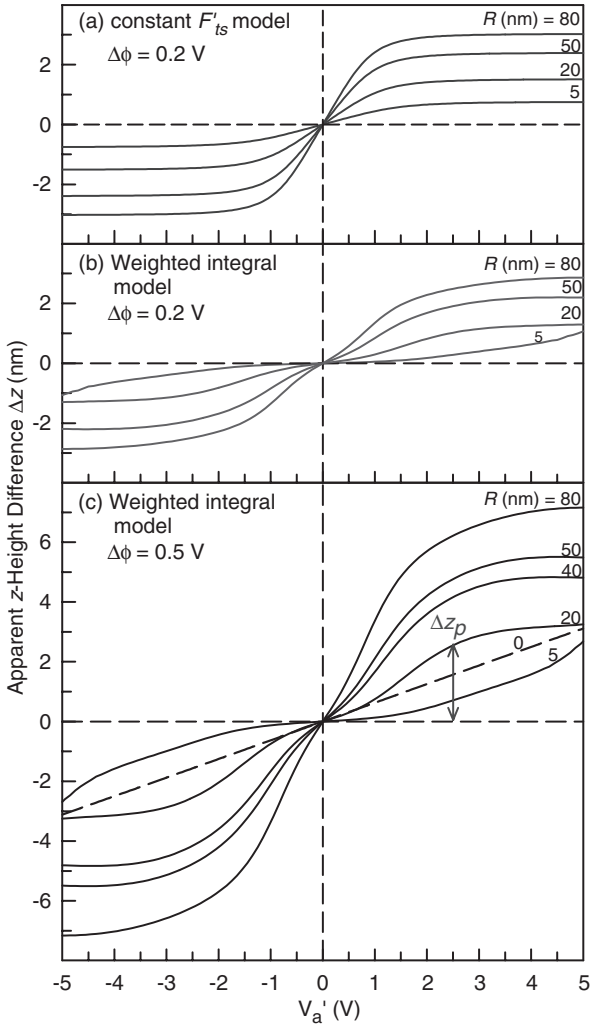

Fig. 4. (a) Calculated apparent topographic height differences Δz for various Rs under obtained scanning conditions. M_1 and M_2 have work function differences $\Delta\phi$ of (a) 0.2 and (b) 0.5 eV. In (c), the double-arrow-labeled Δz_{p} indicates the height difference plateau.

When $R = 0$, the tip has a pure cone shape. The dashed Δz curve shown in Fig. 4(c) has a constant slope, in agreement with a previous study for this special case.[6] For tips with a small radius, the V-independent van der Waals force is the main source of the frequency shift and the tip z-height slightly changes at the M_1–M_2 domain boundary. For tips with $R \gtrsim 20$ nm, $\Delta z(R, V'_{\mathrm{a}})$ initially rapidly increases with V, but gradually reaches a plateau at $V'_{\mathrm{a}} \gtrsim 2$ V. This is once again due to the dominant role of the electrostatic force from the tip. $\Delta z(R, V'_{\mathrm{a}} = 2.5\,\mathrm{V})$ is set for the plateau height Δz_{p}, since F_{apex} dominates around this bias. Δz_{p} is plotted in Fig. 5 for both the simplified constant F'_{ts} model and the comprehensive weighted integral model. As shown in Fig. 5, the plateau height increases with R and $\Delta\phi$. The two models

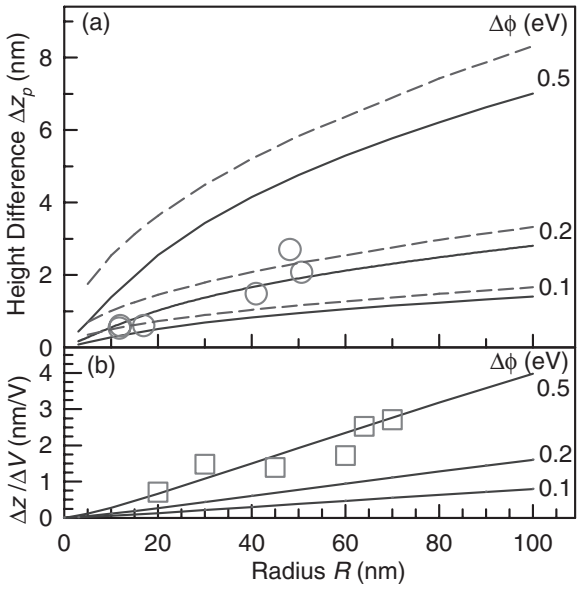

Fig. 5. (a) Plateau height Δz_p measured over flat, differentially doped silicon surface with $\Delta\phi = 0.2$ eV (open circles) and calculated for comprehensive weighted integral model (solid curves) and simplified constant-force-gradient model (dashed curves) for 0.2 and 0.5 V. (b) Average change in topographic height per volt in $|V| < 1$ V obtained by NC-AFM measurement over void depth on oxidized Si(111) surfaces (open squares) and weighted integral calculation (solid curves).

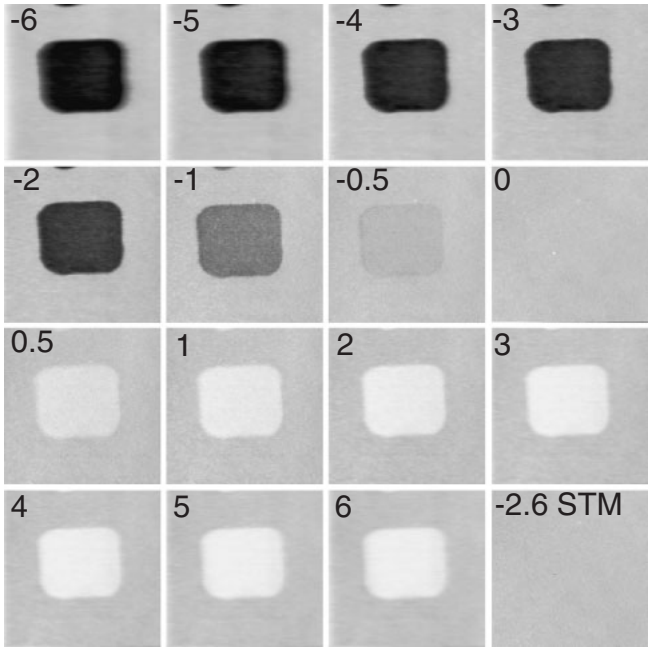

Fig. 6. STM (lower right) and NC-AFM images (others) of H-terminated Si(100) substrate for various tip biases. The size of the images is $6 \times 6\,\mu m^2$ and the range in height is 7 nm. The $3 \times 3\,\mu m^2$ area near the center of each image is n-doped and surrounded by B-implanted p-doped areas. The frequency shift Δf is -30 Hz.

provide similar trends, except that the simplified constant model shows a notably larger Δz_p than the weighted integral model in the case where the two domains have a large work function difference.

3.4 *Experimental observation*

3.4.1 *Results obtained over flat, differentially doped silicon surface*

Figure 6 shows the STM and NC-AFM images with a typical PrIr-coated cantilever. Each $6 \times 6\,\mu m^2$ image in Fig. 6 includes a $3 \times 3\,\mu m^2$ area near the center, which is clearly visible in most of the images. This is an area that is masked off during implantation and remains n-doped. The surrounding area is p-doped by implantation. The lack of contrast in the lower right STM images shows that the surface is topographically flat. The central n-doped region appears topographically lower (higher) than the surrounding areas with a negatively (positively) biased tip, and the height difference depends on the magnitude of the bias voltage.

These variations are caused by varying electrostatic forces. The apparent height differences between the n- and p-doped regions, $\Delta z(R, V_a')$, are deduced from the experiment and the calculations for various bias voltages, and are plotted in Fig. 3(c). The contact potential difference ($\Delta\phi \simeq 0.2$ eV) used for the calculations is obtained from the relative V_a shift between the two measured $D(R, V)$ vs V_a [not shown here, but similar to those in Fig. 3(b)] and/or Δf vs V_a curves over the n- and p-regions. Similar values of contact potential difference were reported earlier and the obtained results were attributed to the effects of the surface and adsorbate-induced states.[19,20] The tip radii Rs in this study were obtained independently from the best fit of the calculated $D(R, V)$ vs V_a curves to that obtained *in situ*. They are in good agreement with manufacturer's specifications and/or our own measurements with an electron microscope. The plateaus of the z-height deviations $\Delta z_p(R, \Delta\phi)$ measured over the same flat, differentially doped silicon surface obtained using several tips are plotted in Fig. 5(a) and are in reasonable agreement with the results obtained by model calculation.

3.4.2 *Results obtained over thin silicon oxide film with voids*

Figure 7(a) shows the NC-AFM image of the oxidized Si(111) surface. The topographic profile indicated by the dashed curves in Fig. 8(a) shows a two-layered step height of $\sim$0.31 nm. This is expected since the top surface layer is uniformly oxidized and the tip–surface interaction is nominally homogeneous. At an elevated temperature, the oxide layer is known to decompose by forming volatile SiO molecules.[21] The ultrathin oxide layer with mostly amorphous SiO_2 requires more Si atoms from the underlying substrate to form SiO molecules, and as a result, thermal desorption followed by surface mass transport typically forms voids of bilayer depth, as shown in Figs. 7(b) and 7(c) and illustrated in Fig. 8(b).

Figure 9 shows three sets of STM and NC-AFM images for surfaces prepared similarly to that in Fig. 7(b). Each set was obtained by careful scanning using the same cantilever (labeled Tip I–III) without a marked change in tip shape. A few oxide voids could be discerned in each image. The relative tip height profiles over the dashed lines and minimum tip–sample distance curves D at spots above Si areas were also measured as a function of tip bias while maintaining a constant Δf and are shown in Figs. 8(c)–8(e) and Fig. 2(b), respectively. The void depths d_{void} were obtained from the NC-AFM images and are shown in Fig. 10.

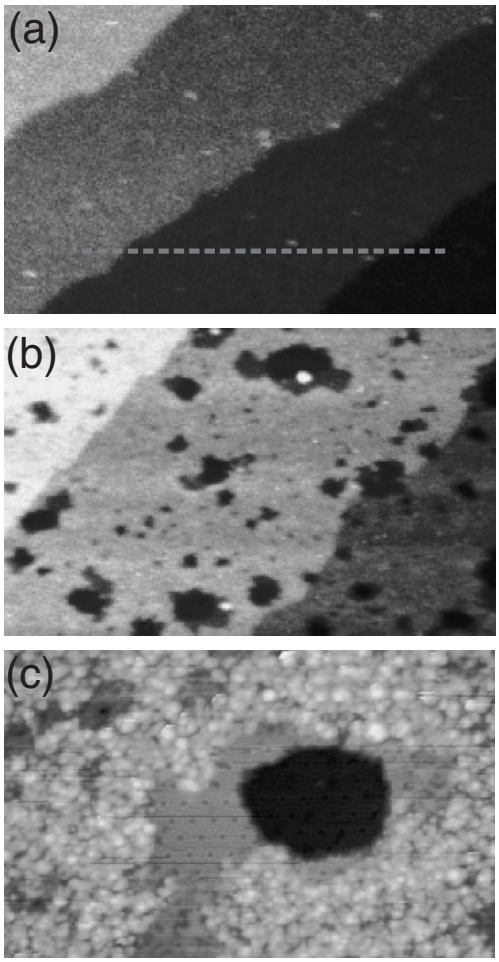

Fig. 7. (a) NC-AFM image of Si(111) surface with ultrathin oxide obtained with $V_a = 1.7$ V and $\Delta f = -50$ Hz. The terraces are separated by 0.31 nm bilayer steps; size: $300 \times 190\,\text{nm}^2$. (b) Same surface after 180 s annealing at ~1020 K; size: $300 \times 190\,\text{nm}^2$. (c) STM image for the same surface with (b). $V_a = -2$ V; size: $80 \times 50\,\text{nm}^2$.

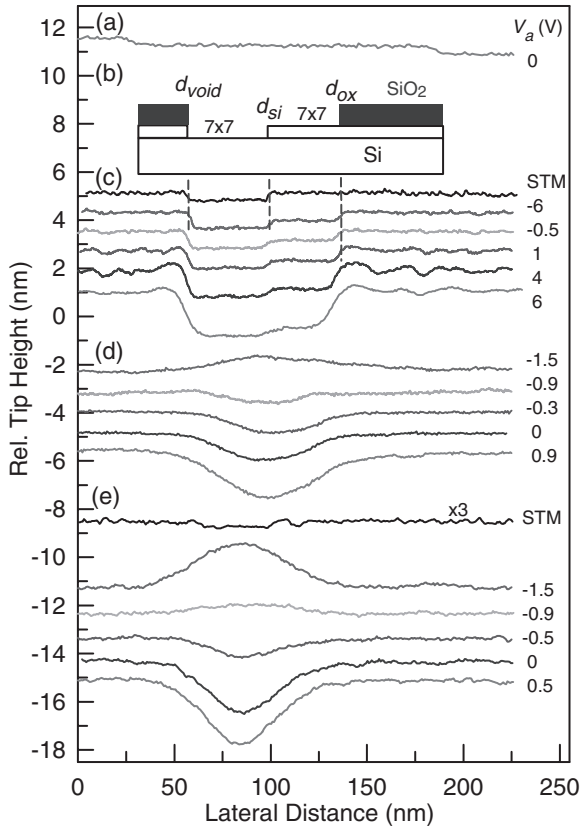

Fig. 8. (a) Line profile over Si(111) surface with thermal ultrathin oxide $V_a = 0$ and $\Delta f = -60$ Hz. (b) Schematic illustration of thermal decomposition of ultrathin oxide layer on Si(111) along with surface mass transport. The oxide layer removal creates a void that typically consists of two terraces with a (7×7) structure and is separated by a bilayer step. (c–e) Relative z-height profiles along dash lines for tips I–III in Fig. 10 with various tip biases. The reduced lateral resolution for tips II and III is due to their large tip–sample distances resulting from a relatively sizeable apex, as evident in their D–V curves in Fig. 2(b).

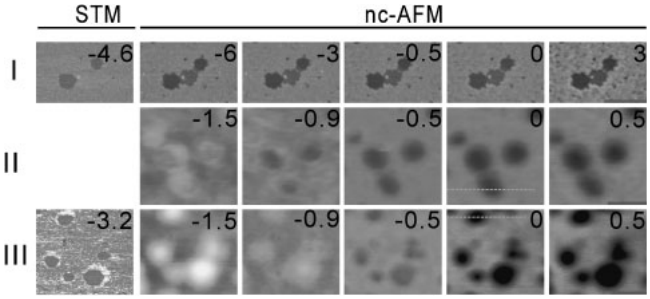

Fig. 9. STM (first column) and NC-AFM images of surfaces similarly prepared to that in Fig. 8(b) with various V_a's. The range in height of these images is 5.5 nm. Row I was obtained with a heavily doped silicon tip. Rows II and III were obtained with PtIr-coated silicon tips. $\Delta f = -30$ Hz.

The first row in Fig. 9 shows the NC-AFM images of an elongated thermal void using an untreated sharp Si tip (labeled I). In Fig. 8(c), all line profiles from the STM and NC-AFM images across the same path indicate $d_{si} = 0.31$ nm for the bilayer step separating the two terraces with a 7×7 structure in the void. This is expected since the tip–surface interaction remains the same when the tip moves across the step between two identical terraces and only shifts the topological step height in both STM and NC-AFM. The presence of these bilayer steps serves as an ideal *in situ* calibration for the z-height measurement, and the *in situ* calibration makes this sample system very favorable for this study. As evident from its line profile [top curve in Fig. 8(c)], the apparent step height (d_{ox}) obtained by STM is nearly zero. This is because the bias is set near the barrier height difference between the vacuum and the oxide, and the work function of tungsten is about 4.5 eV.[22,23] In contrast, the measurements of d_{ox} for the same step between the remaining oxide layer and the first (7×7)-structured layer underneath vary with the tip bias.

As shown in the NC-AFM images in Fig. 9, tip I, an untreated silicon tip, gives rise to low-contrast variations for voids with the potential difference $|V| \lesssim 2$. The tip–sample distance curve obtained using tip I, as shown in Fig. 2(b), is very flat. These observations suggest that the change in electrostatic force is insignificant for a small potential difference. The presence of the van der Waal force and a simultaneous reduction in electrostatic force from the tip apex can be attributed to the existence of a native oxide layer that effectively reduces the capacitance force by enlarging the effective separation between the tip electrode and the sample: $F_{ts}(z) = F_{vdW}(z) + F_{es}(z + t_{ox})$, where t_{ox} is the oxide thickness on the tip apex and $(z + t_{ox})$ is the effective tip electrode–sample separation. We confirmed the existence

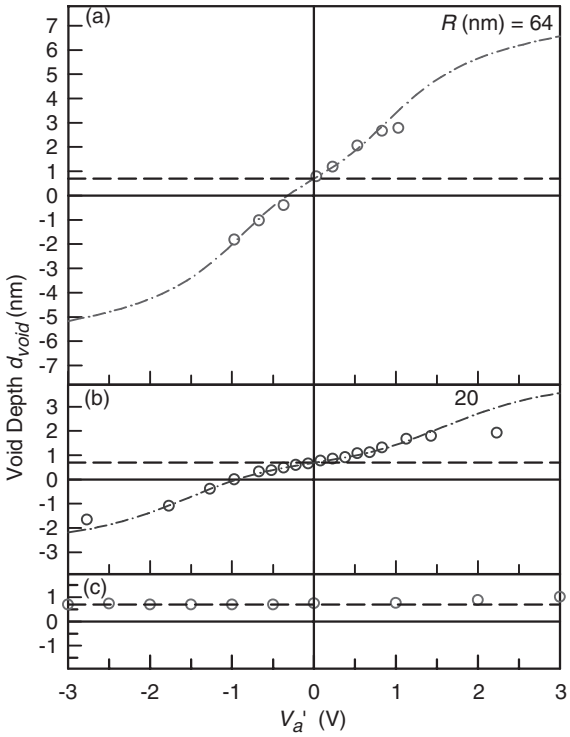

Fig. 10. Void depths measured using tips (a) III, (b) II, and (c) I. $V_a' \equiv V_a + V_b + V_{mcp}$ is chosen so that d_{void} is correctly measured at $V_a' = 0$.

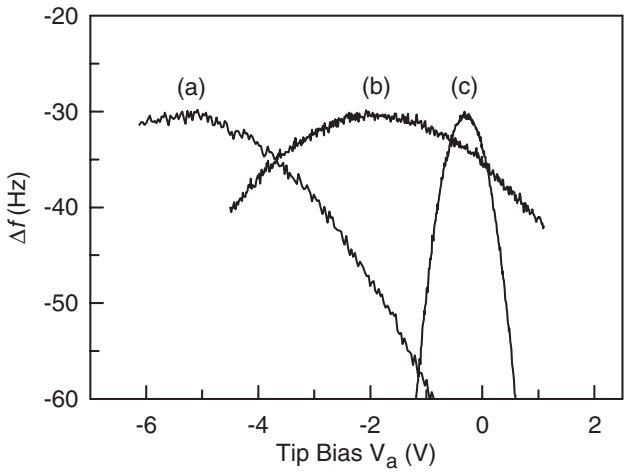

Fig. 11. Frequency shift vs bias voltage curves for (a) untreated Si tip and same tip after (b) controlled gentle scratching and (c) STM-mode operation. The shift in the horizontal position of the curve apex is due to the reduction in effective built-in bias V_b caused by stray charges in the thin native oxide layer.

of a thin oxide layer by controlled tip scratching and STM field evaporation. After gradually removing the thin oxide layer, which is typically a few nanometer thick, stray charges disappear and the effective built-in potential V_b decreases to zero, as observed in the frequency shift vs bias voltage curves (Fig. 11). After the removal of the oxide layer, both the curvature of the $\Delta f(V_a)$ curves and the image contrast variations are enhanced because the tip becomes blunter and/or the effective separation between the tip electrode and sample decreases.

Comparing the first row in Fig. 9 with the other two rows shows that the contrast variations are substantially large for a blunt metallic tip, and the oxide "voids" imaged using PtIr-coated tips II and III appear as humps with large negative biases. These variations are caused by varying electrostatic forces. Figure 2(b) shows that the minimum tip–sample distance curve for tip III has a larger curvature than that for tip II, suggesting that tip III has a larger tip apex than tip II. The void depth obtained from the AFM images are denoted by circles in Fig. 10. The apex radii R for various tips can be again obtained independently by best fitting the measured $D(R, V)$ curves to those solved from eq. (3.3) [such as those in Fig. 2(b)] with the best fit R. The radii found by this method are also in good agreement with manufacturer's specifications and/or our own measurements with an electron microscope.

From the $D(R, V)$ and $\Delta f(R, V_a)$ curves, the contact potential difference, or equivalently $\Delta\phi$, of $\sim$0.5 V was obtained between the silicon and silicon–oxide surfaces. The calculated apparent void depth curves are shown in Fig. 10 and are in agreement with the measurement when V_a' is small. For blunter tips, the voids observed in the NC-AFM images lack resolution. Note that the average diameters of the voids are compatible to that of tip III and that the contact potential of the blunt tip over the small silicon areas is no longer local at a large D, but instead is an average of the silicon and oxide regions. Therefore, the d_{void} curves such as those in Figs. 10(a) and 10(b) do not reach a plateau. Thus, the topographic height variation per volt, that is, $\Delta z/\Delta V$, as a function of R is denoted by squares in Fig. 5(b). As shown in Fig. 5, the result obtained by model calculation is in reasonable agreement with the measurement, and therefore, it can be used for the estimation of Δz when the tip radii and contact potential difference are obtained *in situ* from the $D(R, V)$ curves of the two materials.

4. Conclusions

Noncontact atomic force microscopy is a powerful tool for obtaining nanoscale surface topographic images for semiconductor, biological, and ceramic material structures. However, the topographic height measurement on surfaces with domains of different materials is typically incorrect owing to the variation in capacitive force between a tip and a sample. We performed a detailed theoretical and experimental study of the response of an atomic force microscope operated in frequency-modulated noncontact mode. With two test-sample systems, we experimentally examined the effects of work function variations on the apparent topographic height as a function of the radius, bias, and conductive state of the tip. The obtained results show large topographical variations with seemingly complex functional relationships, but they are well explained by full analysis accounting for all essential interactions in the systems. It is understood that correct topographic measurements on surfaces with more than three materials can only be obtained when the local contact potential V_{cp} is measured and compensated actively during topographic imaging. When the simultaneous contact potential measurement and its compensation are not performed, the results of our analysis indicate that the errors in height measurement can be reasonably estimated by the *in situ* measurement of the work function difference and tip radius.

Acknowledgements

This work is supported by the National Science Council of Taiwan, under Contract No. NSC 95-2112-M009-039 (DSL), and Center for Nano Science and Technology, National Chiao-Tung University (DSL). Dr. Yang would like to thank Professor S. Morita for hosting his summer visit sponsored by Interchange Association, Japan.

1) E. Meyer, H. J. Hug, and R. Bennewitz: *Scanning Probe Microscopy: The Lab on a Tip* (Springer, Berlin, 2003).
2) *Noncontact Atomic Force Microscopy*, ed. S. Morita, R. Wiesendanger, and E. Meyer (Springer, Berlin, 2002).
3) M. Lee and W. Jhe: Phys. Rev. Lett. **97** (2006) 036104.
4) F. J. Giessibl: Rev. Mod. Phys. **75** (2003) 949, and references therein.
5) S. Sadewasser and M. Ch. Lux-Steiner: Phys. Rev. Lett. **91** (2003) 266101.
6) S. Sadewasser, Ph. Carl, Th. Glatzel, and M. Ch. Lux-Steiner: Nanotechnology **15** (2004) S14.
7) R. Bennewitz, A. S. Foster, L. N. Kantorovich, M. Bammerlin, Ch. Loppacher, S. Schär, M. Guggisberg, E. Meyer, and A. L. Shluger: Phys. Rev. B **62** (2000) 2074.
8) S. Morita, M. Abe, K. Yokoyama, and Y. Sugawara: J. Cryst. Growth **210** (2000) 408.
9) Y. Rosenwaks, R. Shikler, Th. Glatzel, and S. Sadewasser: Phys. Rev. B **70** (2004) 085320.
10) R. Dianoux, F. Martins, F. Marchi, C. Alandi, F. Comin, and J. Chevrier: Phys. Rev. B **68** (2003) 045403.
11) E. M. Muller and J. A. Marohn: Adv. Mater. **17** (2005) 1410.
12) D. A. Luh, T. Miller, and T. C. Chiang: Phys. Rev. Lett. **79** (1997) 3014.
13) M. Guggisberg, M. Bammerlin, Ch. Loppacher, O. Pfeiffer, A. Abdurixit, V. Barwich, R. Bennewitz, A. Baratoff, E. Meyer, and H. J. Güntherodt: Phys. Rev. B **61** (2000) 11151.
14) J. Colchero, A. Gil, and A. M. Baró A M: Phys. Rev. B **64** (2001) 245403.
15) L. Olsson, N. Lin, V. Yakimov, and R. Erlandsson: J. Appl. Phys. **84** (1998) 4060.
16) G. M. Sacha, A. Verdaguer, J. Martínez, J. J. Sáenz, D. F. Ogletree, and M. Salmeron: Appl. Phys. Lett. **86** (2005) 123101.
17) M. S. Jean, S. Hudlet, C. Guthmann, and J. Berger: J. Appl. Phys. **86** (1999) 5245.
18) J. N. Israelachvili: *Intermolecular and Surface Forces* (Academic, London, 1991).
19) C. Loppacher, U. Zerweck, S. Teich, E. Beyreuther, T. Otto, S. Grafström, and L. M. Eng: Nanotechnology **16** (2005) S1.
20) A. Kikukawa, S. Hosaka, and R. Imura: Appl. Phys. Lett. **66** (1995) 3510.
21) H. Watanabe, K. Fujita, and M. Ichikawa: Appl. Phys. Lett. **70** (1997) 1095.
22) K. Fujita, H. Watanabe, and M. Ichikawa: J. Appl. Phys. **83** (1998) 3638.
23) K. Fujita, H. Watanabe, and M. Ichikawa: J. Appl. Phys. **83** (1998) 4091.
24) H. Ueyama, Y. Sugawara, and S. Morita: Appl. Phys. A **66** (1998) S295.